



HAL
open science

Experimental characterization of the intragranular strain field in columnar ice during transient creep

Fanny Grennerat, Maurine Montagnat, Olivier Castelnau, Pierre Vacher,
Hervé Moulinec, Pierre Suquet, P. Duval

► **To cite this version:**

Fanny Grennerat, Maurine Montagnat, Olivier Castelnau, Pierre Vacher, Hervé Moulinec, et al..
Experimental characterization of the intragranular strain field in columnar ice during transient creep.
Acta Materialia, 2012, 60 (8), pp.3655-3666. 10.1016/j.actamat.2012.03.025 . hal-01207398v1

HAL Id: hal-01207398

<https://hal.science/hal-01207398v1>

Submitted on 24 Apr 2012 (v1), last revised 30 Sep 2015 (v2)

HAL is a multi-disciplinary open access archive for the deposit and dissemination of scientific research documents, whether they are published or not. The documents may come from teaching and research institutions in France or abroad, or from public or private research centers.

L'archive ouverte pluridisciplinaire **HAL**, est destinée au dépôt et à la diffusion de documents scientifiques de niveau recherche, publiés ou non, émanant des établissements d'enseignement et de recherche français ou étrangers, des laboratoires publics ou privés.

Experimental characterization of intragranular strain field in columnar ice during transient creep

F. Grennerat^{a,*}, M. Montagnat^a, O. Castelnau^b, P. Vacher^c, H. Moulinec^d, P. Suquet^d, P. Duval^a

^aLGGE UMR5183, CNRS / UJF - Grenoble 1, Saint-Martin d'Hères, France

^bProcédés et Ingénierie en Mécanique et Matériaux, CNRS, Arts & Métiers ParisTech, 151 Bd de l'hôpital, 75013 Paris, France

^cLaboratoire SYMME, Université de Savoie, domaine Universitaire BP 80439, 74944 Annecy le Vieux Cedex, France

^dLaboratoire de Mécanique et Acoustique, 31, chemin Joseph Aiguier, 13402 Marseille cedex 20, France

Abstract

A Digital Image Correlation (DIC) technique has been adapted to polycrystalline ice specimens in order to characterize the development of strain heterogeneities at an intragranular scale during transient creep deformation (compression tests). Specimens exhibit a columnar microstructure so that plastic deformation is essentially 2-D with few in-depth gradients, and therefore surface DIC analyses are representative for the whole specimen volume. Local misorientations at the intragranular scale were also extracted from microstructure analyses carried out with an automatic texture analyzer before and after deformation. Highly localized strain patterns are evidenced by the DIC technique. Local equivalent strain can reach values as high as one order of magnitude larger than the macroscopic average. The structure of the strain pattern does not evolve with strain in the transient creep regime. Almost no correlation between the measured local strain and the Schmid factor of the slip plane of the underlying grain is observed, highlighting the importance of the mechanical interactions between neighboring grains resulting from the very large viscoplastic anisotropy of ice crystals. Finally, the experimental microstructure was introduced in a full-field FFT polycrystal model; simulated strain fields are in good match with experimental ones.

Keywords: Elasto-visco-plasticity, polycrystal, creep, strain heterogeneities, Digital Image Correlation

1. Introduction

The deformation of polycrystalline materials gives rise to the build up of heterogeneous stress and strain fields inside individual grains (*intragranular* scale) but also between adjacent grains (*intergranular* scale). These field heterogeneities originate from the anisotropic mechanical behavior of individual grains which is responsible for complex mechanical interactions between adjacent grains upon macroscopic specimen loading. They have a large influence on the overall material response, *e.g.* as illustrated by [1] for the yield stress of elasto-plastic polycrystals.

The development of stress and strain heterogeneities has been studied in a number of papers by making use of full-field numerical approaches [2, 3, 4, 5, 6, 7]. It has been observed that field heterogeneities increase

quickly with the anisotropy of the local constitutive relation. A similar dependence to the nonlinearity is expected, *i.e.* heterogeneities blow up when the local behavior becomes strongly nonlinear [8]. It can also be mentioned that these trends are recovered by mean-field models based on homogenization theories [9].

On the experimental side, local strain can be characterized by means of Digital Image Correlation (DIC) techniques. The method is based on the acquisition of successive images of the specimen surfaces at different strain increments. The comparison of these images allows identifying the displacement field at the specimen surface, which can be then derived to obtain the strain field of interest. This has been the subject of several studies on different metallic alloys exhibiting equiaxed and small (*i.e.* micrometer range) grains [10, 11, 12], in which the systematic development of localization bands at about 45° from the tensile angle and extending along several grain sizes, has been observed. In these studies, the interpretation of strain localization is limited by the unknown microstructure of grains underneath the spec-

*Corresponding Author

Email address:

fanny.grennerat@lgge.obs.ujf-grenoble.fr (F. Grennerat)

imen free surface [11, 13]. To our knowledge, application of DIC to geomaterials has been carried out so far on argillaceous rock [14], soft rock [15] and marble [16].

In this work, DIC technique is applied to polycrystalline ice. This material exhibits a number of specific characteristics that can be used advantageously to gain understanding of polycrystal behavior:

- Large specimens exhibiting columnar microstructures with centimetric grain size can be elaborated. Due to the absence of through-thickness microstructure gradients, fields measured at the specimen surface are representative of the whole specimen volume.
- Ice single crystals exhibit a single easy slip plane for dislocations; the viscoplastic anisotropy is therefore huge at the grain scale. Contrarily to most hexagonal materials, twinning is not an active deformation mode, leading to a relatively simple behavior. The grain response can thus be characterized by a single Schmid factor, compared to many more for cubic or hexagonal metals.

Consequently, since the complete specimen microstructure and main active slip systems are known, one can also anticipate an easier interpretation of results.

This work is focussed on the evolution of strain localization during the transient creep regime, corresponding to overall strain smaller than 10^{-2} . In that regime, the progressive development of an internal stress field is at the origin of the severe decrease of strain-rate [17, 18]. As for geophysical applications, the transient creep of polycrystalline ice is of interest *e.g.* for the behavior of ice shelves submitted to ocean tides [19, 20] and for the heat production within icy satellites [21, 22].

This paper is organized as follows. Section 2 is devoted to the description of the specimen elaboration technique and obtained columnar microstructures. In section 3, adaptation of the DIC technique to our sample configuration is described. The experimental resolution is estimated for the displacement and strain fields. Main results in terms of macroscopic strain and strain fields evolution are given in section 4. Specific results that can be inferred from these columnar microstructure are discussed in section 5. The relation between local strain and local grain orientation is analyzed. Results are also compared to predictions obtained by full-field modeling based on the FFT approach of [23].

2. Columnar ice specimens

2.1. Ice behavior

Ice exhibits a hexagonal crystal structure. The elastic anisotropy of ice single crystals is small, the Young's modulus E varying by about 30% depending on the direction of the loading axis with respect to the c axis. The highest value is along the c axis with $E = 11.8$ GPa at -16°C [24].

The single crystals deform plastically essentially by glide of dislocations on the basal plane. There are three equivalent $\langle 1\bar{2}10 \rangle$ directions for the Burgers vector, but slip in the basal plane is almost isotropic owing to the small stress sensitivity $n = 2$ for basal slip. At similar strain-rates, the equivalent stress requested for non-basal slip is about 60 times larger than for basal slip [25].

For ice polycrystals deformed under the laboratory conditions considered in this work (strain rate lower than 10^{-6} s^{-1} and temperature higher than -15°C), strain is essentially due to intracrystalline dislocation glide [25]. The transient creep regime is characterized by a strong directional hardening until the strain-rate minimum is reached for an overall strain of $\sim 1\%$. This strain-rate decrease can reach three orders of magnitude; it is associated to the development of a strong internal stress field [17, 25, 26]. In the secondary creep regime, isotropic polycrystals deform (at similar stress levels) ~ 100 times slower than a single crystal optimally oriented for basal slip. The corresponding stress sensitivity is close to 3. At strain larger than 1 to 2% (tertiary creep regime), dynamic recrystallization is predominant, and new grain microstructures and crystal orientations are generated [27, 28, 29, 30]. For a review on ice behavior, see [31].

2.2. Elaboration of columnar ice

Samples are made from distilled water slowly frozen under a vertical temperature gradient. The cold room is kept at 0°C while the negative temperature of the recipient bottom is adjustable. The water is constantly stirred by a motorized system to avoid the formation of air bubbles in the growing ice. The growth-rate of solid ice, controlled with the temperature gradient, determines the final grain size. Large growth-rate produces smaller grains. In order to obtain columns with a nearly constant cross section, it was necessary to gradually decrease the table temperature from -10°C to -15°C during the freezing process. An ice layer of 60 mm thickness was grown within about 9h. Columnar specimens with nearly parallel ($\pm 15^\circ$) grain columns was thus obtained (figure 1). The chosen mean grain size (~ 7 mm)

is a good compromise in order to (i) obtain nearly parallel grain columns, (ii) get only one grain in the sample thickness, (iii) reach reasonable intragranular resolution with DIC technique, and (iv) get enough grains in the whole specimen so that the sample size possibly approaches the one of a Representative Volume Element (RVE).

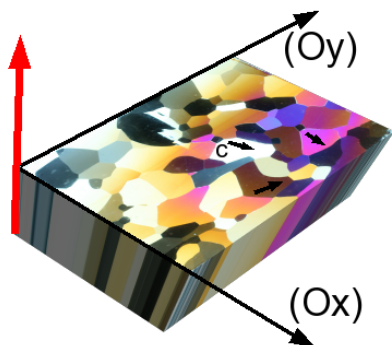


Figure 1: Elaboration of columnar ice under a vertical temperature gradient. The red arrow indicates the ice growing direction, following this gradient.

2.3. Microstructure characterization

Thin sections (~ 0.25 mm thickness) of the specimen are cut before and after deformation to characterize the microstructure with an automatic ice texture analyzer [32]. This is an optical system using polarized light that provides a map of c -axis orientations with a spatial resolution of $43 \mu\text{m}$ and an angular precision of 1° . In the thin section coordinate system (Oxyz), \mathbf{c} is given by coordinates $(\sin \phi \cos \theta, \sin \phi \sin \theta, \cos \phi)$ with θ the azimuth and ϕ the colatitude. From these orientation data, size and spatial distribution of grains can be obtained. Most of the results presented here are extracted from a sample containing 243 grains, with a mean grain size of $5.7 \mu\text{m}$. Its microstructure is shown in figure 2. The sample crystallographic texture is partly provided by the $\{0002\}$ pole figure, see figure 3. Most of the \mathbf{c} -axes are lying close to the sample surface plane : the average and standard deviation of the colatitude are respectively 89.8° and 29.8° . One can therefore anticipate that plastic strain will occur essentially within the XY plane.

As already discussed, grain orientation can be advantageously characterized by a single Schmid factor m_s . For uniaxial compression along direction Y , it reads

$$m_s = \sin \phi \sin \theta (1 - \sin^2 \phi \sin^2 \theta)^{1/2}. \quad (1)$$

Hereafter, m_s will be used only as a convenient *geometrical* criterion for characterizing grain orientation, and

is not associated to any assumption on stress uniformity within grains, not expected here. A large Schmid factor ($= 0.5$) corresponds to a \mathbf{c} -axis at 45° from the macroscopic compression direction; it vanishes for \mathbf{c} -axes either parallel or perpendicular to that direction. Schmid factor values are superimposed on the initial specimen microstructure in figure 2. Uniform values within grains reveal the very small intragranular misorientation, smaller than the detection limit of the texture analyser.

2.4. Mechanical tests

Uniaxial compression creep tests are performed in a cold room at $-12 \pm 1^\circ\text{C}$ under a constant stress of 0.5 MPa and for $\sim 50\text{h}$, to reach $\sim 1\%$ overall strain (figure 4). Such a maximum strain level was chosen to stop the test in the secondary creep regime, just before the tertiary creep dominated by dynamic recrystallization. Samples are machined in the lab with high geometrical accuracy to parallelepipedic shape of dimensions close to $90 \text{ mm} \times 90 \text{ mm} \times 15 \text{ mm}$ (height \times width \times thickness). Two teflon sheets are placed between the sample and the press in order to avoid friction at the specimen contact surfaces. It has been verified, on a specimen with very fine grains and exhibiting isotropic behavior (randomly oriented and equiaxed grains), that load is uniformly applied on the specimen surface, with no friction, since in that case the displacement field measured by DIC is linear with x and y as expected for homogeneous specimens [33]. The other surfaces of the sample are stress free.

The overall deformation of the sample along the compression direction Y is measured with a LVDT (Low Voltage Displacement Transducer), positioned to record the whole specimen length changes.

2.5. Superimposition of strain and microstructure maps

In order to superimpose the strain fields obtained by the DIC technique with the specimen microstructure, two holes ($\phi = 1\text{mm}$) are drilled in the sample next to its corners, before sampling the initial thin section. This enables a superimposition with a maximum error of a few pixels, *i.e.* $\sim 0.2 \text{ mm}$. However, as discussed below, this accuracy is limited in practice by the inclination of grain boundaries that are not exactly parallel to the Z axis, and by the ice total thickness required for thin section elaboration ($\sim 2 \text{ mm}$). Based on these uncertainties, we estimate that the superimposition of strain and microstructure maps is accurate within $\sim 0.5 \text{ mm}$.

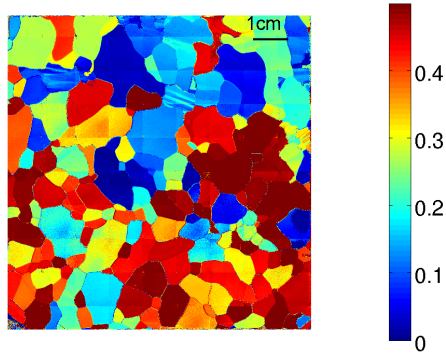


Figure 2: Specimen microstructure measured with the automatic texture analyzer, before deformation. The color scale indicates the Schmid factors that have been calculated from the c -axis orientation data. On this map, the squared pattern of 1cm size is an artefact from the analyzer.

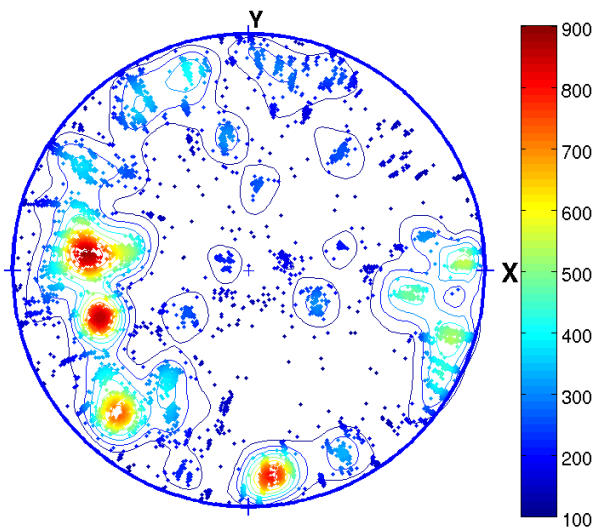


Figure 3: Pole figure of the c -axes, before specimen deformation. Data points coming from the texture analyser are indicated by dots. The color code indicate the pole figure intensity (arbitrary units). Y corresponds to the macroscopic compression direction.

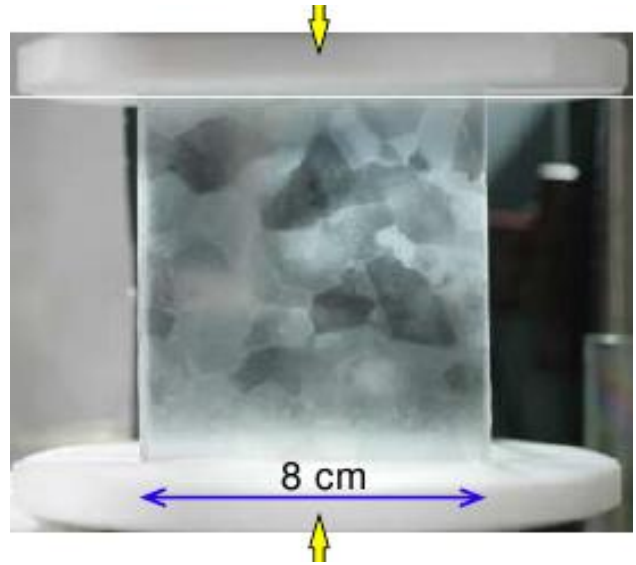


Figure 4: Setup for uniaxial compression tests. Individual grains can be detected thanks to cross polarizers.

3. DIC setup and resolution

Digital Image Correlation technique relies on three steps: (i) speckle patterns are applied on the sample surface, (ii) successive images of the speckle pattern are taken along the deformation of the sample, and (iii) correlation between successive images is performed to measure surface displacements. The displacement resolution depends on those three steps, *i.e.* the quality of the speckle, the optical setup and the correlation procedure. In the present study use was made of the software 7D described in [34]. Technical details about the optical setup are given in the appendix.

3.1. Speckle deposition and characterization

Speckle deposition on ice is an issue for two reasons. First, use of toxic products is not allowed in cold rooms, and most of the regular substances used to create speckle patterns (paint, ink, ...) do not adhere on the ice surface. Second, the ice surface is sublimating rapidly in the cold room at -12°C . After several attempts, the best solution was obtained by applying a small layer of shoe polish after having slightly polished the ice surface with sandpaper to improve the cohesion of the speckle. A typical example of speckle pattern is shown in figure 5.

Texture parameters of the speckle were studied following [35, 36]. The mean standard deviation of the speckle of figure 5 is $\sigma \approx 22.5$ gray levels. This value has to be large enough to improve the subpixel resolution of the

displacement in DIC measurements ; if $\sigma > 6$ gray levels, then a resolution of 0.01 pixels [36] can be reached. The autocorrelation radius of the speckle, which provides an average feature size [36], is obtained by averaging, in every direction, the length at half the maximum of the correlation. For most of our samples, the values were found between 3.7 and 7.4 pixels. From [35], the optimal value stands between 3 and 5 pixels. Therefore, for the highest values of the radius, our speckle pattern is over-sampled and a larger subset size will be required during matching. In these conditions, the spatial resolution that is achievable is slightly reduced.

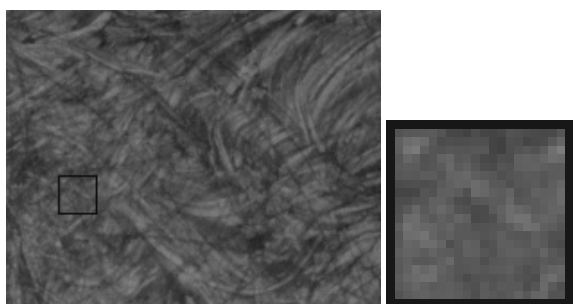


Figure 5: Typical speckle pattern (left) and zoom on a 20×20 pixels window (right).

3.2. DIC resolution

A virtual grid is associated with the initial image with a step of $n \times n$ pixels, and at each grid node a correlation window (also called pattern size) of size $p \times p$ pixels is defined. In each correlation window, interpolation of grey levels enable the estimation of displacements with a subpixel (ideally 0.01 pixels) accuracy [35, 37]. Here, a bilinear interpolation of the grey levels was used. The resulting displacement field is interpolated with a bilinear form on each element of the grid, and differentiated by a finite difference scheme to obtain the strain field.

As for sizes n and p , compromises have to be made. The size of the correlation window p determines the spatial resolution, which must be adapted to the actual strain heterogeneities to be characterized. p should be large enough to keep significant grey level gradients in the correlation window. The best spatial resolution that can be achieved is associated with the correlation radius r and the standard deviation of the speckle [35, 36]. On the other hand, the smaller the step grid n , the worse the strain resolution. Here, values $p = n = 20$ pixels were selected. This corresponds to a spatial resolution of 1.2 mm, *i.e.* small enough compared to the grain size to reach intragranular resolution.

Resolution of the DIC setup depends on many factors. Effect of the overall image noise has been estimated by correlating many (~ 10) images acquired successively without any specimen motion nor setup change. Unlike the no-motion theoretical result, the DIC technique identifies slight (artificial) specimen deformations. The mean standard deviation measured for component ε_{yy} was 0.16%.

In an attempt to evaluate systematic errors associated with subpixel displacements (so-called ‘S curve’) the method proposed by [38] was used. Successive images of the fixed specimen were taken for small camera translations along the optical axis. Application of DIC to the set of images should lead to a purely radial displacement field with an increasing amplitude from the image center to the edges. DIC subpixel errors can be estimated as the difference from this theoretical solution. Unfortunately, camera motion could not be generated properly enough, with unavoidable slight camera rotations, and the obtained translation field was not perfectly radial. However, an upper bound of ~ 0.07 pixels could be determined for subpixel errors [33].

Out-of-plane specimen motion is another source of error for 2-D DIC setups. This effect has been estimated by applying a stereo-correlation technique [39] to a specimen exhibiting a similar microstructure as the one presented here. Thanks to the use of a second camera at some angle from the first one, out-of-plane motion can be estimated [40]. Although this setup introduces important additional issues due to light reflection and pixel saturation, it could be checked that after deformation, the sample surface was slightly wavy but with wavelengths of the same order as the specimen size. The standard deviation of the out-of-plane displacement was $\sigma_z = 0.15$ mm over the whole surface. This value has to be compared with the distance between the camera lens and the sample surface (900 mm) for the estimation of the associated deformation error, which standard deviation is then $\sim 0.017\%$ ($= 0.15/900$).

4. Results

4.1. Strain response

The overall specimen response under compressive creep loading is shown in figure 6. The average axial deformation based on DIC measurements is obtained from the relative displacement between the top and bottom parts of the specimen. There is a good match with strain measurements obtained by the LVDT; the slight discrepancy is probably due to the fact that the LVDT is not centered on the loading axis. For this specimen,

secondary creep regime is reached after $\sim 70\text{h}$ for an axial strain of $\sim -1\%$.

The evolution of strain heterogeneities measured by DIC is presented in figure 7. Maps of local equivalent strain obtained after -0.32% , -0.62% and -0.85% macroscopic axial strain are shown. Here, the equivalent strain is defined as $\varepsilon_{eq} = \sqrt{\frac{2}{3}(\varepsilon_{xx}^2 + \varepsilon_{yy}^2 + 2\varepsilon_{xy}^2)}$. This definition does not account for components ε_{xz} , ε_{yz} , and ε_{zz} , not measured with our setup, but at the same time these components are expected to remain very small compared to ε_{xx} , ε_{yy} , and ε_{xy} due to the particular orientation of the grain \mathbf{c} -axis (it has been checked that the effective strain $\bar{\varepsilon}_{zz}$ is only about 15% the value of $\bar{\varepsilon}_{yy}$ indicating that, at least macroscopically, out-of-plane strain remains small). The deformation tends to concentrate into bands inclined with respect to the applied stress direction, which width is smaller than the grain size. This deformation pattern appears at an early stage of deformation, and does not evolve significantly with strain. For the three deformation stages shown in figure 7, local strain values reach up to ten times the macroscopic average. But recall that strain evaluated by DIC is an average over n pixels (here $\approx 1.2\text{ mm}$), and therefore the very *local* strain values in ice could be much larger than measured here.

Strain statistics, calculated over the whole specimen, can be inferred from these data. As shown in figure 8 computed for $\bar{\varepsilon}_{yy} = -0.85\%$, local strain values are spread over a large range. The equivalent strain is very well fitted by a log-normal distribution with a long tail at high strain, highlighting again the strong strain localization. Such a distribution already appears at the early stage of the transient creep test. Interestingly, distribution of the axial component ε_{yy} shows a significant positive part although the average value $\bar{\varepsilon}_{yy}$ is negative; local tensile strain arises in the specimen compressed at the macroscopic scale. Similar conclusion can be drawn for component ε_{xx} . The shear component distribution ε_{xy} is approximately symmetric and slightly narrower than axial components.

To characterize the statistical orientation of localization bands at the specimen scale, covariance of the strain field was calculated, following [41]. For this, we made use of the normalized correlation function

$$C(\mathbf{h}) = \frac{\int_S \varepsilon_{eq}(\mathbf{x})\varepsilon_{eq}(\mathbf{x} + \mathbf{h})dS}{\int_S \varepsilon_{eq}^2(\mathbf{x})dS} \quad (2)$$

with S the considered surface, and \mathbf{x} and \mathbf{h} two position vectors. This relation requires periodicity of the strain map and no correlation of strain for distances larger than the image size. To perform the calculations, strain maps

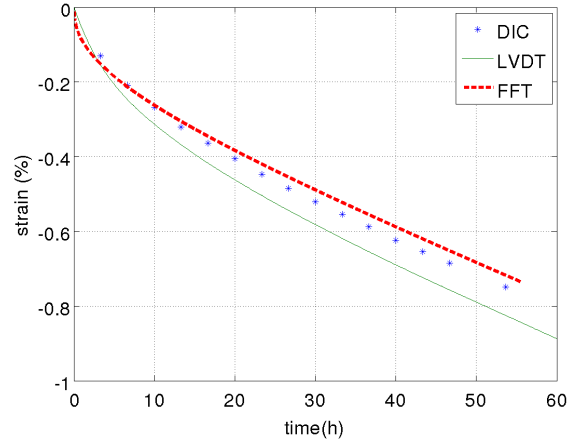


Figure 6: Overall specimen response. DIC contour average is compared with LVDT measurements and with the prediction from the FFT modeling (see part 5.2).

have been padded with their mean value, so that the considered surface S is a square of length twice the largest dimension of the original map. The covariogram obtained for -0.85% overall strain is presented in figure 9, where the correlation function has been calculated for several directions of \mathbf{h} . We denote χ the angle between \mathbf{h} and sample direction X , and $C_\chi(\mathbf{h})$ the corresponding correlation function. A correlation radius r_χ is then defined as:

$$r_\chi = \text{Min}\{r \geq 0 \mid C_\chi(r) \leq C_\chi^\infty\} \quad (3)$$

with C_χ^∞ the asymptotic value of C_χ at large $|\mathbf{h}|$. The major orientation of localization bands, denoted χ_{max} , corresponds to the value χ for which r_χ is maximum. A value of about -32° was found for the present specimen. This orientation does not evolve with strain, in agreement with the stable position of localization bands. It is worth noting that correlation radius r_χ reaches values up to $\sim 60\text{ mm}$, even at the beginning of the deformation test. This correlation radius provides a measure of the interaction length between the deforming grains, which is thus much larger (by about one order of magnitude) than the mean grain size. Note that it is also very close to sample dimensions (this point is discussed in section 5). A similar analysis was performed on five other samples, revealing band orientations ranging between 30° and 60° , and interaction lengths from 8 to 12 times the mean grain size.

4.2. Link with the microstructure

Superimposition of strain maps with the specimen microstructure was performed with the procedure de-

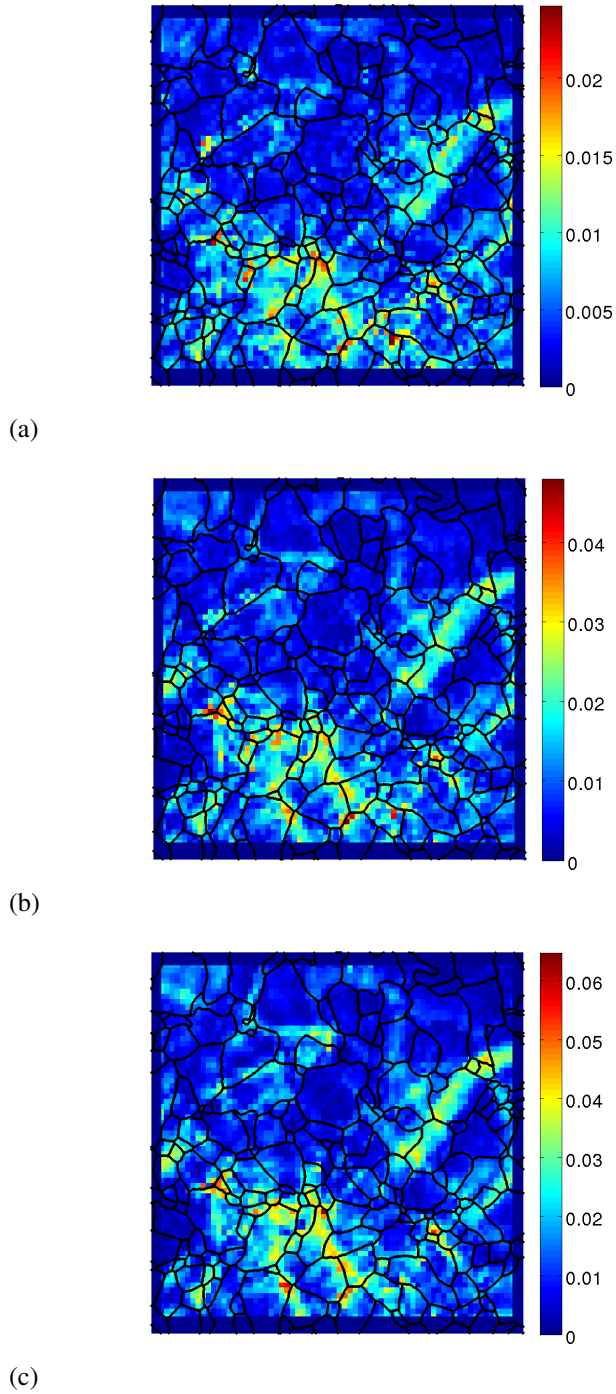


Figure 7: Evolution of the equivalent strain in the transient creep regime, for an axial macroscopic deformation of (a) -0.32% , (b) -0.62% , and (c) -0.85% . Note that the color scales are different. DIC could not be performed up to the specimen very edges; the total specimen size corresponds to the outer blue square.

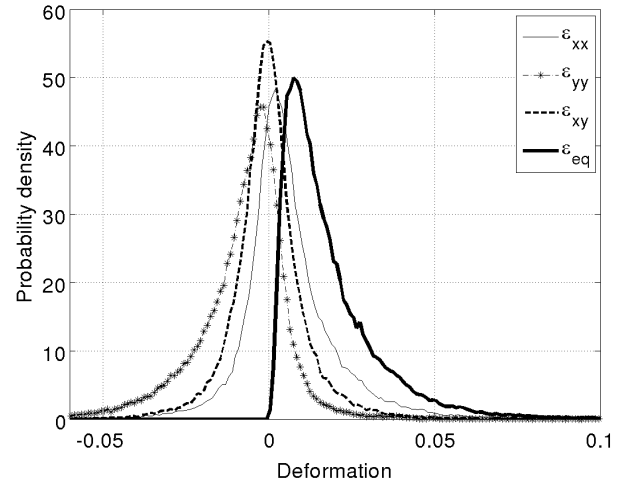


Figure 8: Probability density of the different components of the deformation obtained at -0.85% macroscopic strain.

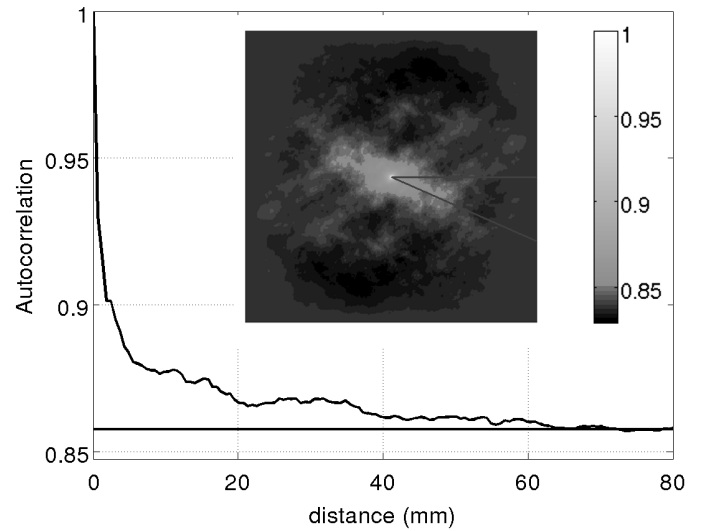


Figure 9: (map) Covariogram of the equivalent strain presented in figure 7c, and (curve) profile of the covariogram for the direction $\chi = -32^\circ$ corresponding to the largest correlation radius.

scribed in section 2.5. Grain boundaries are indicated in figure 7. It can be observed that large localizations are most often encountered next to grain boundaries, but note that this feature is not systematic: large strain can also be observed inside grains, and not all grain boundaries support a localization band. For a more quantitative analysis of the spatial repartition of strain, we took advantage of the actual specific columnar microstructure in which all grain boundaries are nearly perpendicular to the specimen surface. A distance function providing the distance of any pixel to its nearest grain boundary can thus be defined without ambiguity. Results are shown in figure 10 in which, to improve the statistical relevance, we stacked data obtained for five different specimens with similar grain size. The figure clearly shows that strain is more heterogeneous next to grain boundaries than within grain interior. Large strains are observed only in the vicinity of grain boundaries, however pixels next to grain boundaries do not necessarily experience a strain larger than grain interiors. Moreover, on average, strain is probably slightly larger next to grain boundaries but this tendency is rather soft (red least-square line on the figure).

Finally, it is of interest to investigate the relation between the normalized equivalent strain $\varepsilon_{eq}/\bar{\varepsilon}_{eq}$ and the Schmid factor m_s . Recall that ice grains exhibit a single isotropic easy glide slip plane, and therefore the Schmid factor can be unambiguously determined for each grain. For doing this, pixels close to grain boundaries (distance < 0.3 mm) have to be discarded since it cannot be determined to which side of the grain boundary they belong, due to the uncertainties described in section 2.5. Results, normalized by the overall equivalent strain, are presented in figure 11. Surprisingly, unlike the expected trend with ε_{eq} rapidly increasing with m_s , data do not show any specific tendency. A least square regression analysis of these data indicates that the deformation of grain is however slightly increasing with the Schmid factor, although the correlation coefficient is rather small (< 0.2) due to the large spread of data points. To improve the statistical relevance of this result, a similar analysis was performed on five other specimens exhibiting a qualitatively similar microstructure, and a very similar trend as in figure 11 was obtained. The important conclusion is that local grain deformation is not driven by the local Schmid factor. Grains with large Schmid factor, generally considered as ‘soft’ and ‘well oriented’ for glide, do generally not deform more than grains with small Schmid factor. Deformation data for a given value of Schmid tensor show also great variability.

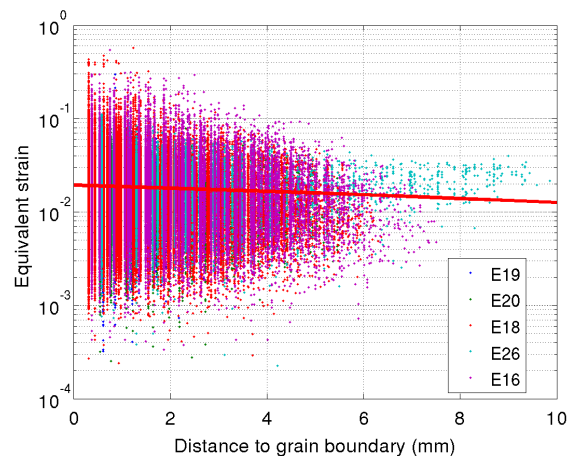


Figure 10: Equivalent strain vs. distance to grain boundaries for a set of five different samples with similar grain size. Each point corresponds to a pixel of the DIC images. Overall strain is $\sim 0.8\%$.

5. Discussion

5.1. Strain distribution

In this experimental study, we adapted the DIC technique to investigate the mechanical response of ice at an intragranular spatial scale, and its evolution during deformation under uniaxial creep. The deposited speckle pattern was optimized so that the whole DIC setup could reach adequate strain and spatial accuracies, that have been evaluated. We took benefit of some unique specificities of this material, namely (i) the possibility of easy elaboration of columnar microstructures with no in-depth gradients, and (ii) the deformation mechanisms with a single easy glide slip system, which is moreover almost isotropic. The distribution of strain has been investigated in relation with the underlying grain microstructure. Huge strain heterogeneities have been evidenced. Local equivalent strain measured by DIC reaches values as high as one order of magnitude larger than the macroscopic average. But recall that strain values measured by the DIC technique are spatial average data, here over ~ 1.2 mm, and therefore the real (local) strain localization is expected to be larger. Thanks to the specific columnar microstructure, the distance of any point within a grain to the nearest grain boundary could be calculated. It was found that grain boundary regions, where the largest strain values are measured, deform in a much more heterogeneous way than grain interiors. Thanks to the specific dislocation slip systems, Schmid factor of grains could also be calculated with no ambiguity. It was found that apparently ‘favorably oriented’ grains (*i.e.* those with a high Schmid

factor) do not necessarily deform more than any other grains. We also stress that very similar results were obtained on many specimens, and therefore these results are not specific to the particular sample presented here.

Observations of the intragranular deformation of ice was already presented in [42, 43, 44, 45] on 2-D microstructures, some of them including ellipsoidal inclusions. The DIC technique was not applied at that time and strain heterogeneities were characterized indirectly through lattice misorientation measurements. Our experimental study suggests that stress is strongly redistributed in the entire specimen during creep loading. The observed strain localization must be associated to strong stress concentrations, with eventually a minor role of local Schmid factors but a strong impact of neighborhood relationship. The creep behavior of *isotropic* polycrystalline ice has been already well documented in [17, 26]. In the present work, due to the specific orientation of *c*-axes lying almost parallel to the specimen surface, the measured strain-rate obtained for the secondary creep (*i.e.* for $\bar{\epsilon}_{eq} \sim 1\%$) is about $3\text{--}8 \times 10^{-8} \text{ s}^{-1}$, in good agreement with what was measured by [46] in similar conditions, and one order of magnitude larger than for isotropic ice with random grain orientation [27]. At the very early stage of loading, the instantaneous specimen response is purely elastic. Since the elastic behavior of ice single crystals is close to isotropic, uniform stress and strain fields are thus expected. Unfortunately, strain field could not be measured by DIC at very small overall strains (elastic strain is $\sim 0.5 \times 10^{-4}$) due to the limited experimental resolution. As plastic deformation comes into play, with the activation of highly anisotropic dislocation glide almost entirely on the basal slip system, stress must be redistributed. According to [25, 17], as grain boundaries act as obstacles to basal slip, creep should relax the resolved stress on the basal plane on each grain and the load should be transferred to stiffer non-basal systems. Dislocation climb and cross-slip can also contribute to the relaxation of directional internal stresses. Transient creep is therefore associated with the development of a long-range internal stress field, responsible for the hardening associated with the large strain-rate decrease. The hardening associated with primary creep is essentially kinematic, and is responsible for the large deformation recovered after unloading [25].

In the deformation maps obtained by DIC, it was observed that strain localization appears at an early stage of creep, *i.e.* for strain as small as -0.32% , with an already developed pattern of localization that does not evolve qualitatively with increasing strain. But, as shown in [26], the development of internal stress field

might be even more rapid; the stress heterogeneity associated with the high local viscoplastic anisotropy starts developing as far as plastic strain exceeds the elastic strain, and should be fully developed for deformation of the order of $5 \cdot 10^{-4}$ [25, 45].

An important result of this study is the relation between grain orientation and local strain. Surprisingly, local strain is only very poorly correlated with the Schmid factor of the unique easy glide slip plane. So-called 'well oriented grains', *i.e.* exhibiting a large Schmid factor, do not necessarily deform more than 'badly oriented grains' (with small Schmid factor). This is in contradiction with simple (intuitive) micromechanical models such as the Reuss (or static) bound assuming stress uniformity within the whole polycrystalline specimen [47], and for which local deformation is entirely determined by the grain orientation. In ice, owing to the very high local viscoplastic anisotropy, the mechanical interaction between neighboring grains is very strong, and therefore the deformation of a specific grain is highly influenced by its neighborhood [48, 45]. Similar conclusions have been drawn for other highly anisotropic materials. In olivine, a mineral exhibiting only three independent easy glide slip systems, full-field numerical approaches show that a correlation is obtained between local equivalent stress (or strain-rate) and grain orientation but only when average is performed over a very large number of grains exhibiting similar grain orientation but different neighborhood [18, 49]. The corollary of this feature is twofold. First, one must be very careful with very simple or *ad hoc* micromechanical models, such as the Reuss bound, for the interpretation of the rheology of highly anisotropic polycrystals. Our results indicate that the activation of slip systems might be very different from such simple predictions. Second, for the interpretation of local observations of the polycrystal deformation, such as with Transmission Electron Microscopy, one should consider the fact that the local stress might be very different from the macroscopic one.

The deformation pattern within the sample is characterized by localization bands which are oriented between 30 to 60° from the compression axis. The length of the deformation bands is about one order of magnitude larger than the grain size, *i.e.* between 50 to 70 mm here, which is also about the sample dimension (about $90 \times 90 \text{ mm}^2$). Therefore, we can expect local deformation mechanisms to interact over a distance much larger than the average grain size. This is coherent with estimation of spatial correlation length of dislocation avalanches found much larger than the grain size [50]. As a consequence, the behaviour is more or less

independent on microscopic effects (grain size). The relation between the equivalent strain and the grain orientation is hidden and only small effect can be detected. The samples of our experiments might however not constitute a representative volume element (RVE), and care must be taken when analyzing the results from one isolated sample. In particular, the dispersion of the deformation pattern characteristics (band orientation and length) could be influenced by this sample size limitation and the particular boundary conditions applied here. Similar deformation band localization were found either experimentally [51, 41, 52, 11] or numerically [11, 48]. In particular, [41] found similar deformation bands forming at an angle of $\pm 52^\circ$ with respect to the tensile direction in Zr with a characteristic length of the strain localization pattern of 5 to 10 times the average grain size. Deformation band patterning during deformation of polycrystalline materials raises the problem of the determination of the RVE from the only observation of the microstructure [11]. Note finally that estimated RVE length scale depends on the measurement resolution used for DIC experiments [13].

Our results indicate that the equivalent strain measured by DIC at different strain levels follows a log-normal distribution. In particular, a small volume fraction of grains deforms significantly more than the polycrystal average. From a computational approach, [53] points out the influence of the non-linearity of the local behavior on the shape of the probability density of the strain fields in 2-phases composites. In particular, the Gaussian distribution was approached only with a linear behavior. Similarly, [7, 54] obtained assymmetric distributions of stress and strain rate from a FFT full-field prediction in the case, respectively, of a viscous-linear aggregate and metal-metal composite materials. Using the same FFT approach, [18] predicted a strong increase of the distribution width with increasing of the local viscoplastic anisotropy of olivine grains. In particular, a bi-modal shear stress distribution was obtained for an easy slip system of a theoretically "soft" crystal orientation; in many grains sharing the same crystal orientation, glide on the same easy slip plane can occur in opposite directions. Such observations clearly evidence the strong impact of neighboring grains on the local stress and strain conditions whose contribution get stronger with an increasing anisotropy.

5.2. Comparison with full-field modeling

Full-field numerical simulations were performed using the FFT method initially proposed by [5, 53], first applied to viscoplastic polycrystals by [6], and extended to elasto-viscoplastic composites using a step-by-step

integration in time by [8] (see also numerical details in [55]). The FFT method consists in finding a strain-rate field associated with a kinematically admissible velocity field that minimizes the average local work-rate under the compatibility and equilibrium constraints. An iterative scheme is used until convergence toward a fixed point. It is numerically more efficient than the Finite Element method [56], however it is limited to microstructures submitted to periodic boundary conditions.

The specimen microstructure detailed in section 2 was discretized into 1024×1024 Fourier points with a single layer of Fourier point in the third (Z) direction, assuming thus infinite column lengths. The experimental *c*-axis orientation was introduced in the model. The exact experimental boundary conditions (stress free lateral surface) could not be reproduced due to the periodicity constraint, therefore fields predicted close to the specimen edges are not expected to be very accurate. As for the local constitutive relation, both the elastic and viscoplastic responses of ice crystals was considered [55]. Crystal plasticity accounts for three different families of slip systems, namely basal, prismatic, and $\langle a \rangle$ -pyramidal systems, the latter two being taken stiffer than basal slip. A standard power law is considered for the slip rate $\dot{\gamma}^{(k)}$ on system (*k*) :

$$\dot{\gamma}^{(k)} = \dot{\gamma}_0^{(k)} \left(\frac{|\tau^{(k)} - X^{(k)}|}{\tau_0^{(k)}} \right)^{n^{(k)}} \text{sign}(\tau^{(k)} - X^{(k)}), \quad (4)$$

with τ^k the resolved shear stress acting on the system (*k*) and $\dot{\gamma}_0^{(k)}$ a reference slip rate taken equal to 10^{-6}s^{-1} . The reference shear stresses τ_0 evolve following a Voce-type law :

$$\dot{\tau}_0^{(k)} = (\tau_{sta}^{(k)} - \tau_0^{(k)}) \dot{p}^{(k)}, \quad \dot{p}^{(k)} = \sum_{\ell=1}^M h^{(k,\ell)} |\dot{\gamma}^{(\ell)}| \quad (5)$$

where $h^{(k,\ell)}$ is a constant hardening matrix. X are backstresses associated to kinematic hardening given by a simple saturating law [57] :

$$\dot{X}^{(k)} = c^{(k)} \dot{\gamma}^{(k)} - d^{(k)} X^{(k)} |\dot{\gamma}^{(k)}| - e^{(k)} X^{(k)}. \quad (6)$$

Parameters of this constitutive relation, which are slightly different than those used in [26], are provided in Table 1, together with $c = 9 \text{ MPa}$, $d = 60$, and $e = 0.0003 \text{ s}^{-1}$. Details about the identification procedure are published in [55].

As shown in figure 6, the model agrees well with the measured overall behavior despite a relatively rapid

	τ_{ini}	τ_{sta}	n	H	Ba	Pr	Pyr
Ba	0.1	0.022	2	Ba	70	125	0
Pr	0.15	1.625	2.85	Pr	125	110	0
Pyr	3.875	3.875	4	Pyr	0	0	0

Table 1: Initial (*ini*) and stationary (*sta*) values of the reference shear stresses $\tau^{(0)}$, stress sensitivity n , and the hardening matrix H (last 3 columns). Values of τ and H are given in MPa.

identification of the above parameters. The predicted strain and stress field after -0.84% macroscopic axial stress are presented in figure 12. It can be observed, by comparison with figure 7, that the general location and orientation of the deformation bands is well predicted, with strain concentration at triple junctions and close to grain boundaries, but also often within grain interiors. The largest predicted local strain is about 10 times the macroscopic equivalent strain, and appears localized in much finer areas than in the experimental observations. This discrepancy has to be associated with the different spatial resolutions, much lower for the DIC results. One can not rule out the probable effects of periodic boundary conditions discussed above, especially since the sample size is rather small compared to the characteristic length of the strain localization pattern. Nevertheless, the overall good match between the localization pattern predicted by FFT and measured experimentally tends to indicate that boundary conditions have a minor influence compared to the mechanical interaction between grains.

The large strain heterogeneity is associated with high concentration of local stresses as shown in figure 12b. With the actual FFT spatial resolution, the local equivalent stress, defined as $\sigma_{eq} = \sqrt{\frac{3}{2}\sigma_{ij}\sigma_{ij}}$, can reach up to 5 times the macroscopic one, but note that there is not a one-to-one correspondance with the local equivalent strain. Small strain values can be associated to either large or small stress, depending on the considered location, in agreement with earlier findings on olivine polycrystals [58]. Sensitivity tests (not presented here) also showed that the resistance of hard prismatic and pyramidal slip systems, and their hardening, has a strong influence on the level of strain heterogeneity. The balance between isotropic and kinematic hardening should also play a role in the simulation of the transient creep kinematics toward secondary creep and will have to be carefully estimated. A more detailed comparison between FFT full-field modeling and DIC results requires a broader study beyond the scope of the present paper. However, the good match already obtained shows that DIC experimental results are solid. In particular, as seen

in figure 11, the lack of correlation between local equivalent strain and grain Schmid factor, observed experimentally, is fully reproduced by the FFT approach.

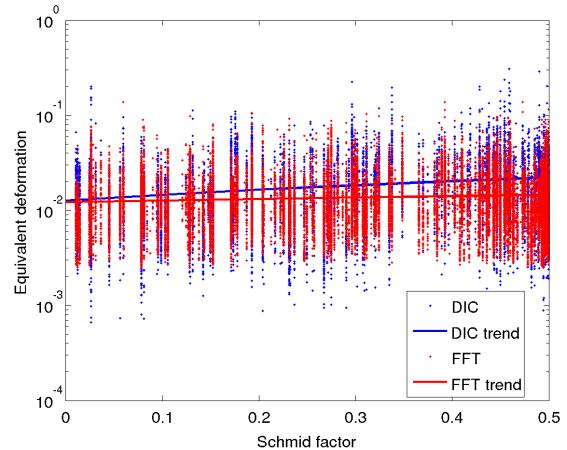


Figure 11: Equivalent strain vs. Schmid factor for macroscopic strain of $\sim -0.7\%$ as obtained by DIC, and compared to FFT predictions (see part 5.2).

6. Summary and conclusions

The strain field was evaluated in ice polycrystals by a Digital Image Correlation technique with an intra-granular spatial resolution. Sample microstructure was essentially 2-D, with columnar grains exhibiting c -axis orientation nearly parallel to the sample plane and little in-depth microstructure gradient, so that plane strain conditions could be approached. Samples were deformed under compression creep, and the strain field evolution was estimated all along the transient creep until about 1% macroscopic axial strain.

The measured strain field is highly heterogeneous with local values up to one order of magnitude larger than the macroscopic strain. It was observed that tensile strains can take place locally in the macroscopically compressed specimen. In grain boundary regions, strain is more heterogeneous than within grain interiors. Strain heterogeneities tend to concentrate into bands similarly to observations for other materials [51, 41, 11]. The length of the bands is ~ 8 times the average grain size, therefore, local deformation mechanisms are expected to interact over a distance larger than the average grain size, and close to the actual sample dimension. Statistical measurements performed over several similar microstructures reveal no clear correlation between grain orientation and strain level. The present experimental results thus do not support the classical

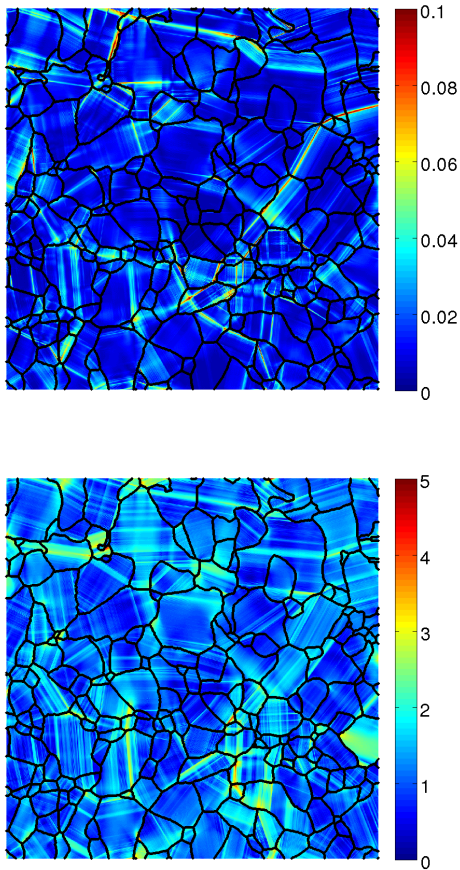


Figure 12: Full-field FFT predictions for the distribution of (a) the equivalent strain, and (b) the equivalent stress, for a macroscopic axial deformation of -0.84% .

model opposing "well oriented" grains to "badly oriented" grains (depending on the local Schmid factor) to explain ice deformation. The strong viscoplastic anisotropy of ice induces strong mechanical interactions between neighbor grains that strongly influence local deformations. Observed strain heterogeneities are well reproduced by the elasto-viscoplastic full-field FFT model in which the experimental microstructure is introduced. In particular, the lack of correlation between local grain orientation and local equivalent strain supports experimental observations.

The experimental measurement of intra-granular strain field developing during transient creep appears as a powerful tool to identify and validate full-field elasto-viscoplastic approaches aiming at representing the material response during complex deformation path. In addition, microstructure evolutions such as local lattice misorientations associated to rapidly appearing kink bands will be further analyzed with respect to local strain and stress fields.

Acknowledgment

This study was partly funded by the French 'Agence Nationale de la Recherche' (project ELVIS, #ANR-08-BLAN-0138). Support by institutes INSIS and INSU of CNRS, and University Joseph Fourier, France, is acknowledged.

Appendix A. DIC optical setup

Ice surface is reflecting light efficiently. To avoid sharp light reflections and saturation of some pixels in the images, the entire device (sample plus press) was covered with a semi-transparent plastic film to scatter all light sources. The sample was illuminated with two lamps, each composed of several white LEDs, positioned about 20 cm away from the sample and behind the plastic film.

For image acquisition, a 21.1-megapixel (3750×5630 pixels) CMOS digital reflex camera (Canon EOS 5D Mark II) with a 180mm f/3.5 macrolens was used. The lens to sample distance was 90 cm, the exposure time 0.6s, the aperture number 10, the ISO value 500, and the focus on manual position to avoid any changes during the experiment. The camera was connected to a laptop, and images were recorded every 20min. With this setup, the pixel size of the correlated images was 0.06 mm. The lens resolution is limited by diffraction features. Diffraction patterns are characterized by the Airy disc radius $r_{Airy} = 0.61 \frac{\lambda}{\alpha}$, where λ is the wavelength of the

LED and α the numerical aperture ($\alpha = \frac{D}{2f} = \frac{1}{2AV}$). For a wavelength of 700nm and the aperture value AV=10, we obtain $r_{Airy} \approx 8.5 \mu\text{m}$, which is way smaller than the super-pixel size ($\sim 60 \mu\text{m}$) as required.

References

- [1] R. Brenner, R. Lebensohn, O. Castelnau, *Int. J. Solids Struct.* 46 (2009) 3018–3026.
- [2] P. R. Dawson, A. J. Beaudoin, *Finite element simulations of metal forming*, in: *Texture and Anisotropy. Preferred orientations in polycrystals and their effect on materials properties*, Cambridge University Press (ISBN 0 521 46516 8), 1998, pp. 297–305.
- [3] D. Mika, P. Dawson, *Acta Mater.* 47 (4) (1999) 1355–1369. doi:10.1016/S1359-6454(98)00386-3.
- [4] F. Barbe, S. Forest, G. Cailletaud, *Int. J. Plast.* 17 (2001) 537–563.
- [5] H. Moulinec, P. Suquet, *Computer Methods in Applied Mechanics and Engineering* 157 (1-2) (1998) 69–94.
- [6] R. A. Lebensohn, *Acta Materialia* 49 (14) (2001) 2723–2737.
- [7] R. Lebensohn, O. Castelnau, R. Brenner, P. Gilormini, *International Journal of Solids and Structures* 42 (20) (2005) 5441–5459.
- [8] M. I. Idiart, H. Moulinec, P. Ponte Castañeda, P. Suquet, *J. Mech. Phys. Solids* 54 (2006) 1029–1063.
- [9] R. Lebensohn, Y. Liu, P. Ponte Castañeda, *Proc. Royal Soc. Lond. A* 460 (2045) (2004) 1381–1405.
- [10] D. Raabe, M. Sachtleber, Z. Zhao, F. Roters, S. Zaefferer, *Acta Materialia* 49 (17) (2001) 3433–3441.
- [11] E. Héripré, M. Dexet, J. Crépin, L. Gélébart, A. Roos, M. Bornert, D. Caldemaison, *Int. J. Plast.* 23 (9) (2007) 1512–1539.
- [12] M. Sutton, N. Li, D. Garcia, N. Cornille, J. Orteu, S. McNeill, H. Schreier, X. Li, A. Reynolds, *Experimental Mechanics* 47 (2007) 789–804, 10.1007/s11340-007-9041-0.
- [13] C. Efstathiou, H. Sehitoglu, J. Lambros, *International Journal of Plasticity* 26 (2010) 93–106.
- [14] M. Bornert, F. Valès, H. Gharbi, D. Nguyen Minh, *Strain* 46 (1) (2010) 33–46.
- [15] T. Nguyen, S. Hall, P. Vacher, G. Viggiani, *Tectonophysics* 503 (1-2) (2010) 117 – 128.
- [16] L. Xu, B. Evans, *Journal of Geophysical Research* 115 (B04202).
- [17] M. F. Ashby, P. Duval, *Cold Reg. Sc. Tech.* 11 (1985) 285–300.
- [18] O. Castelnau, D. K. Blackman, R. A. Lebensohn, P. Ponte Castañeda, *Journal of Geophysical Research* 113.
- [19] A. Jenkins, H. Corr, K. Nicholls, G. Stewart, C. S. M. Doake, *Journal of Glaciology* 52 (178) (2006) 325–345.
- [20] M. A. King, K. Makinson, G. H. Gudmundsson, *Geophys. Res. Lett.* 38.
- [21] T. G. W. J. Sotin C., *Europa after Galileo*, The University of Arizona Press, Tucson, AZ, 2009, Ch. Tides and tidal heating on Europa, pp. 85–118.
- [22] L. Han, A. P. Showman, *Icarus* 212 (1) (2011) 262–267.
- [23] H. Moulinec, P. Suquet, *Compte-rendu de l'Académie des sciences. Série II, Mécanique, physique, chimie, astronomie* 318(11) (1994) 1417–1423.
- [24] P. H. Gammon, H. Kiefte, M. J. Clouter, W. W. Denner, *J. Glaciol.* 29 (103) (1983) 433–460.
- [25] P. Duval, M. F. Ashby, I. Anderman, *J. of Phys. Chem.* 87 (21) (1983) 4066–4074.
- [26] O. Castelnau, P. Duval, M. Montagnat, R. Brenner, *Journal of Geophysical Research Solid Earth* 113 (B11203).
- [27] T. H. Jacka, M. Maccagnan, *Cold Reg. Sci. Technol.* 8 (1984) 269–286.
- [28] S. de La Chapelle, O. Castelnau, V. Lipenkov, P. Duval, *J. Geophys. Res.* 103 (B3) (1998) 5091–5105.
- [29] P. Duval, L. Arnaud, O. Brissaud, M. Montagnat, S. D. L. Chapelle, *Ann. Glaciol.* 30 (2000) 83–87.
- [30] M. Montagnat, P. Duval, *Earth Planet. Sci.* 183 (2000) 179–186.
- [31] P. Duval, M. Montagnat, F. Grennerat, J. Weiss, J. Meyssonier, A. Philip, *Journal of Glaciology* 56 (200) (2010) 1059–1068.
- [32] D. S. Russell-Head, C. Wilson, *J. Glaciol.* 24 (90) (2001) 117–130.
- [33] F. Grennerat, *Hétérogénéités de déformation au cours du fluage transitoire de la glace polycristalline, mesures par corrélation d'images numériques et modélisation*. Ph.D. thesis, Université de Grenoble, France (2011).
- [34] P. Vacher, S. Dumoulin, F. Morestin, S. Mguil-Touchal, *Proc Instn Mech Engrs* 213 (1999) 811–817.
- [35] M. Sutton, J. Orteu, H. Schreier, Springer (ISBN 978 0 387 78746 6), 2009.
- [36] K. Triconnet, K. Derrien, F. Hild, D. Baptiste, *Optics and Lasers in Engineering* 47 (2009) 728–737.
- [37] H. Louche, K. Bouabdallah, P. Vacher, T. Coudert, P. Baland, *Experimental Mechanics* 48 (2008) 741–751.
- [38] D. S. Yang, M. Bornert, H. Gharbi, P. Valli, L. L. Wang, *EPJ Web of Conferences* 6.
- [39] L. Robert, F. Nazaret, T. Cutard, J.-J. Orteu, *Experimental Mechanics* 47 (2007) 761–773, 10.1007/s11340-007-9062-8.
- [40] T. Coudert, *Reconstruction tridimensionnelle du volume intérieur d'une chaussure, évaluation du chaussant*, Ph.D. thesis, Université de Savoie (2005).
- [41] P. Doumalin, M. Bornert, J. Crépin, *Mécanique et Industries* 4 (2003) 607–617.
- [42] P. Mansuy, J. Meyssonier, A. Philip, Berlin, etc. Springer-Verlag, (Lecture Notes in Physics) 533 (1999) 215–224.
- [43] P. Mansuy, A. Philip, J. Meyssonier, *Ann. Glaciol.* 30 (2000) 121–126.
- [44] P. Mansuy, J. Meyssonier, A. Philip, *Computational Materials Science* 25 (1-2) (2002) 142–150.
- [45] M. Montagnat, J. R. Blackford, S. Piazzolo, L. Arnaud, R. A. Lebensohn, *Earth and Planetary Science Letters* 305 (1-2) (2011) 153–160.
- [46] O. Plé, *Contribution à l'étude de l'endommagement de la glace colonnaire S2 en compression uniaxiale*, Ph.D. thesis, Université Joseph Fourier-Grenoble I (1998).
- [47] U. F. Kocks, C. N. Tomé, H. Wenk, *Texture and Anisotropy. Preferred orientations in polycrystals and their effect on materials properties*, Cambridge University Press (ISBN 0 521 46516 8), 1998.
- [48] R. Lebensohn, M. Montagnat, P. Mansuy, P. Duval, J. Meyssonier, A. Philip, *Acta Materialia* 52 (18) (2009) 5347–5361.
- [49] O. Castelnau, R. Lebensohn, R. Brenner, A. Rollett, *Acta Mater.* 56 (15) (2008) 3914–3926.
- [50] T. Richeton, J. Weiss, F. Louchet, *Dislocation avalanches: role of temperature, grain size and strain hardening*, *Acta Mater.* 53 (2005) 4463–4471.
- [51] F. Delaire, J. L. Raphanel, C. Rey, *Acta Mater.* 48 (5) (2000) 1075–1087.
- [52] L. Gélébart, J. Crépin, M. Dexet, M. Sauzay, A. Roos, *J. ASTM Int* 1 (2004) JAI12333.
- [53] H. Moulinec, P. Suquet, *European Journal of Mechanics - A/Solids* 22 (5) (2003) 751–770.
- [54] S.-B. Lee, R. Lebensohn, A. Rollett, *International Journal of Plasticity* 27 (5) (2011) 707–727.
- [55] P. Suquet, H. Moulinec, O. Castelnau, M. Montagnat, N. Lahellec, F. Grennerat, P. Duval, R. Brenner, *Procedia Iutam*.

- [56] A. Prakash, R. Lebensohn, *Simul. Mater. Sci. Eng.* 17 (2009) 1–16.
- [57] J. L. Chaboche, *Int. J. Plast.* 24.
- [58] O. Castelnau, P. Cordier, R. A. Lebensohn, S. Merkel, P. Rateron, C. R. *Physique* 11 (2010) 304–315.